The DOI for this manuscript is doi: 10.1175/MWR-D-15-0036.1

Bayesian Exploration of Multivariate Orographic Precipitation Sensitivity for Moist Stable and Neutral Flows

Samantha A. Tushaus*

Space Science and Engineering Center, Madison, WI, USA

Derek J. Posselt

University of Michigan, Ann Arbor, MI, USA

M. Marcello Miglietta

Institute of Atmospheric Sciences and Climate (ISAC), Italian National Research Council (CNR), Lecce, Italy

Richard Rotunno, Luca Delle Monache

National Center for Atmospheric Research, Boulder, CO, USA

* *Corresponding author address*: Samantha A. Tushaus, Space Science and Engineering Center, University of Wisconsin-Madison, 1225 W. Dayton Street, Madison, WI 53706-1612. Email: sam.tushaus@ssec.wisc.edu

Abstract

Recent idealized studies examined the sensitivity of topographically forced rain and snowfall to changes in mountain geometry and upwind sounding in moist stable and neutral environments. These studies were restricted by necessity to small ensembles of carefully chosen simulations. Research presented here extends earlier studies by utilizing a Bayesian Markov chain Monte Carlo (MCMC) algorithm to create a large ensemble of simulations, all of which produce precipitation concentrated on the upwind slope of an idealized Gaussian bell-shaped mountain. MCMC-based probabilistic analysis yields information about the combinations of sounding and mountain geometry favorable for upslope rain, as well as the sensitivity of orographic precipitation to changes in mountain geometry and upwind sounding. Exploration of the multivariate sensitivity of rainfall to changes in parameters also reveals a non-unique solution: multiple combinations of flow, topography, and environment produce similar surface rainfall amount and distribution. Finally, the results also divulge that the non-unique solutions have different sensitivity profiles, and that changes in observation uncertainty also alter model sensitivity to input parameters.

1. Introduction

More than half a century of orographic precipitation research has discovered that topographically forced rainfall is sensitive to mountain shape, three-dimensional winds, surface properties, the characteristics of the upstream sounding, and details of cloud microphysical processes (Sawyer 1956; Smith 1979; Barcilon et al. 1979; Durran and Klemp 1982, 1983; Miglietta and Buzzi 2001; Colle 2004). In many regions, large-scale moist stable and neutral flow is instrumental in generating upslope precipitation in mountainous terrain (Douglas and Glasspoole 1947; Sawyer 1956; Sarker 1967; Doswell et al. 1998; Buzzi and Foschini 2000; Rotunno and Ferretti 2003; Miglietta and Rotunno 2005, 2006). This type of flow has been recently analyzed as *atmospheric rivers* interacting with orography along the U.S. West Coast (Ralph et al. 2004; Ralph et al. 2005; Niemann et al. 2011; Ralph and Dettinger 2011; Rutz et al. 2014).

A number of field campaigns have been conducted with the goal of improved understanding of stable and moist neutral orographic precipitation. Precipitation along the United States Intermountain West and mountainous West Coast was the focus of the PACific Land-falling JETs campaign (PACJET; Niemann et al. 2002), the Improvement of Microphysical PaRameterization through Observational Verification Experiment (IMPROVE and IMPROVE-II; Stoelinga et al. 2003), the Intermountain Precipitation EXperiment (IPEX; Schultz et al. 2002), and the Sierra Hydrometeorology Atmospheric Rivers Experiment (SHARE; Kingsmill et al. 2006). The Mesoscale Alpine Programme (MAP; Bougeault et al. 2001; Rotunno and Houze 2007) observed storm systems and moist flow impinging on the European Alps. All of these studies confirmed that mesoscale orographic effects on airflow determine the location, intensity, and amount of observed rainfall. Rotunno and Ferretti (2003) reported on two intensive

observing periods in MAP that observed nearly moist-neutral stability during the passage of synoptic storm systems. In addition, Rotunno and Houze (2007), in a MAP summary paper, recommended a thorough exploration of the orographic precipitation parameter space to better understand its sensitivity to changes in upstream conditions. Their findings and the broader outcomes of MAP motivated a number of numerical modeling studies, including the idealized studies of Miglietta and Rotunno (2005, 2006, 2009, 2010; hereafter MR05, MR06, MR09, and MR10, respectively).

These idealized studies showed that the complex interrelationship between controlling atmospheric and topographic factors and resulting orographic precipitation makes it difficult to clearly discern (1) which combinations of factors produce a given distribution of precipitation, and (2) how multiple simultaneous changes in the thermodynamic sounding, flow, and mountain geometry enhance or suppress precipitation. MR05 and MR06 examined the sensitivity of steady-state orographic precipitation in moist neutral flow to changes in temperature profile, mountain height and width, and cloud microphysics complexity. They classified their rainfall distributions into categories according to mountain height. However, classification became difficult as mountain width and profile temperature were allowed to vary, implying complexity in the relationships between mountain geometry, the upwind sounding, and resulting surface precipitation.

While MR05 and MR06 focused on moist neutral flow, a scenario adequately characterized by a two-dimensional framework, conditionally unstable flows are more complex (MR09; MR10; Miglietta and Rotunno 2012, 2014). They are associated with a succession of three-dimensional, time-dependent cloud cells, which together may be considered a class of turbulent flow. MR09 and MR10 examined the role of buoyancy in determining surface

precipitation by conducting 80 numerical experiments with varying values of convective available potential energy (CAPE) and downdraft CAPE (DCAPE), wind speed, and mountain height and width. They discovered a complicated relationship between the chosen control parameters and precipitation, one that changed depending on the region of parameter space examined. Studies of both stable and unstable flows indicate that controls on orographic precipitation are multivariate, and an exploration of the connections between different factors of influence will require a more complete exploration of parameter (co)variability than has previously been attempted.

In this paper we extend the analysis of MR05 and MR06 to address two fundamental science questions concerning precipitation generated by moist neutral flow over a barrier:

1. What is the quantitative sensitivity of topographically forced precipitation to changes in mountain geometry, wind profiles, and the thermodynamic environment?
2. Which combinations of physical states and mountain configurations produce a given distribution and intensity of upslope precipitation?

Both questions can be answered by systematically varying the factors that control upslope precipitation in a cloud system resolving model and examining the results. The challenge is the computational expense of examining every parameter permutation necessary to thoroughly explore multivariate sensitivity in the orographic precipitation system. We surmount this challenge using a Bayesian methodology, supplemented by a stochastic sampling procedure (section 2), to answer our research questions in a systematic and objective manner. We outline our results in detail in section 3, provide further discussion and analysis in section 4, and summarize our major conclusions in section 5.

2. Numerical Methods

97 *2.1 CM1 Model*

98 The Cloud Model 1 (CM1) described in Bryan and Fritsch (2002)
99 (http://www2.mmm.ucar.edu/people/bryan/cm1) was designed for study of cloud-scale
100 atmospheric processes. It uses the vertically implicit, time-splitting Klemp-Wilhelmson
101 technique to calculate the non-hydrostatic compressible equations of mass, momentum, energy,
102 and moisture. A fifth-order advection scheme operates in the horizontal and vertical for both
103 scalars and velocities. CM1 uses a terrain-following vertical coordinate, and subgrid-scale
104 turbulence is parameterized using a turbulent kinetic energy closure (Deardorff 1980).

105 While ice microphysical processes are known to exert a significant effect on orographic
106 precipitation (Stoelinga et al. 2003), parameterizations are highly sensitive to assumed ice
107 density, particle shape, and fall speed (Posselt and Vukicevic 2010). This research represents the
108 first time a complete multivariate orographic precipitation sensitivity analysis has been
109 conducted. As such, and for simplicity, we consider only liquid processes in our experiments and
110 utilize a warm-rain (Kessler 1969) scheme. Tests of various CM1 simulations in moist stable and
111 neutral conditions revealed that the model reaches a steady precipitation distribution after
112 approximately 10 simulated hours (MR05, MR09). While three dimensions and 1 km grid
113 spacing, or finer, are typically required to model deep convection (Bryan et al. 2003), moist
114 neutral flow can be realistically simulated using a two-dimensional domain and 2 km grid
115 spacing (MR05, MR06). The simulations in this study are performed with CM1, release 17, and
116 have a 2D domain 800 km in length. The minimum number of grid points (three) was used in the
117 y-direction, as CM1 does not run in parallel in purely 2D mode. Horizontal grid spacing is 2 km
118 and stretches to 6 km over 50 grid points at each end of the x-domain. The domain is 20 km in
119 height with 59 vertical levels. The vertical grid spacing is 250 m from the surface to z = 9,000 m,

120 increases to 500 m from z = 9,000 m to z = 10,500 m, and stays constant at 500 m above
121 z = 10,500 m (as in MR05). Lateral boundary conditions are all open-radiative, the lower
122 boundary is free-slip, and a Rayleigh damping layer is applied to the top 6 km of the domain to
123 prevent reflection of vertically propagating gravity waves. Comparisons between the
124 configuration described above and a reference simulation run with 250 m horizontal and vertical
125 grid spacing produced nearly identical results (not shown).

126 In this study, the flow characteristics, cloud properties, and resulting precipitation amount
127 and distribution are governed by only six parameters: mean wind speed (ū), squared moist Brunt-
128 Väisälä frequency (N_m^2), surface potential temperature (θ_{sfc}), profile relative humidity (RH),
129 mountain height (H_{mtn}), and mountain half-width (W_{mtn}). As with the microphysics, for
130 simplicity mean wind speed and direction, relative humidity, and N_m^2 are constant with height at
131 the upwind boundary. Precipitation is binned into six regions on the mountain: three each on the
132 upwind and downwind slopes (Fig. 1). Initial conditions consist of an idealized moist neutral
133 sounding (MR05), continuously advected into the domain from the west (upwind) boundary (Fig.
134 2). An idealized bell-shaped mountain is constructed from the same function used in MR05,
135 MR06, MR09, and MR10, where mountain height is defined as

136 $$h(x) = \frac{h_m}{1 + [(x - x_0)/a]^2}. \quad (1)$$

137 Here x is the position within the domain in meters, the mountain is centered on x_0, h_m is
138 maximum mountain height, and a is the mountain half-width in meters. The mountain height and
139 half-width parameters control the mountain geometry.

140 *2.2 Sensitivity Analysis, Bayes Theorem, and MCMC Algorithms*

141 The fundamental goals of this study are to (1) explore which combinations of mountain
142 geometry and upwind sounding parameters result in similar orographic precipitation amount and
143 spatial distribution, and (2) assess the sensitivity of precipitation to changes in sounding and
144 mountain geometry. If precipitation expresses particular sensitivity to changes in wind speed, for
145 example, in theory a narrow range of wind speed values will define a given precipitation
146 distribution. A challenge comes in the form of *mitigating factors*; for example, an increase in
147 wind speed may be compensated by a decrease in relative humidity in order to produce
148 equivalent water vapor-to-precipitation conversion rates. If only a few factors control
149 precipitation rate, it is straightforward to assess the parameter-precipitation relationship and the
150 sensitivity of precipitation to parameter changes using successive numerical model runs.
151 However, for more than 3-4 controlling parameters, the computational challenge of simulating
152 precipitation for every possible combination of parameters (*brute force sensitivity analysis*)
153 becomes impractical. In fact, the computational expense grows as M^N, where M is the number of
154 discrete values of input parameters and N is the number of parameters.
155 We may reduce the computational burden by realizing that some model runs from the
156 brute force sensitivity analysis do not produce a precipitation distribution similar to the
157 distribution of interest. As in an optimization problem, we seek sets of input parameters that fit a
158 given precipitation distribution while avoiding sets of input parameters with a poor fit. However,
159 unlike an optimization problem, the search for sets of input parameters must allow for the
160 possibility of multiple solutions, or multiple parameter sets that produce an equally good fit to
161 the given precipitation distribution. *Markov chain Monte Carlo* (MCMC) *algorithms* comprise a
162 class of Bayesian methods that explore a parameter space and assess model output sensitivity,
163 while avoiding parameter sets that produce a poor fit to the chosen observations.

Let a set of upwind sounding and mountain geometry parameters be represented in a six-element vector $\mathbf{x} = [\bar{u}, N_m^2, \theta_{sfc}, RH, H_{mtn}, W_{mtn}]$, and let the given precipitation distribution (binned into six mountain regions) be represented in a six-element vector $\mathbf{y}$ = [P1,P2,P3,P4,P5,P6]. All input parameters in $\mathbf{x}$ are assigned realistic ranges, outlined in Table 1, with equal (Uniform) probability of occurrence. A CM1 simulation with a specified set of control parameters (Table 1) produces the given precipitation distribution $\mathbf{y}$ (values in Table 2). Our fundamental goals may now be expressed as (1) exploring which values of $\mathbf{x}$ produce a given precipitation distribution $\mathbf{y}$, and (2) assessing the sensitivity of $\mathbf{y}$ to changes in the input parameters $\mathbf{x}$. Exploring the probability of $\mathbf{x}$ given $\mathbf{y}$, or $P(\mathbf{x}|\mathbf{y})$, allows us to quantify the probability that a certain set of parameters $\mathbf{x}$ produces the given precipitation distribution $\mathbf{y}$, and use the probability density function $P(\mathbf{x}|\mathbf{y})$ to describe the sensitivity of precipitation $\mathbf{y}$ to input parameters $\mathbf{x}$. Bayes' Theorem defines $P(\mathbf{x}|\mathbf{y})$:

$$P(\mathbf{x}\,|\,\mathbf{y}) = \frac{P(\mathbf{y}\,|\,\mathbf{x})P(\mathbf{x})}{P(\mathbf{y})} \quad . \tag{2}$$

$P(\mathbf{x})$ is the Bayesian *prior*, which represents our knowledge of the elements of $\mathbf{x}$ before $\mathbf{y}$ is known. In our study $P(\mathbf{x})$ corresponds to a bounded Uniform probability of occurrence for each possible value of the parameters in $\mathbf{x}$; no combination of parameters is more likely than any others within the provided range. $P(\mathbf{y}|\mathbf{x})$, termed the *likelihood*, represents the probability that the simulated precipitation rates $\mathbf{y}$ produced by a given set of parameters $\mathbf{x}$ are equivalent to the precipitation rates calculated in the control simulation, and takes into account measurement uncertainty. In essence, the likelihood quantifies how close the simulated precipitation rates are to those produced by the control run. If parameter set $\mathbf{x}$ produces rain rates $\mathbf{y}$ that are very close to those in the control run, the likelihood will be large, and vice versa. We have defined the

186 precipitation rate standard deviation as 2 mm hr^{-1}, and assumed a Gaussian distribution for the
187 likelihood. Note that one may assume other probability distributions for the likelihood, such as
188 the Log-Normal distribution used in Posselt et al. (2008). $P(\mathbf{y})$ is a normalizing factor that
189 integrates over all possible precipitation rates **y** produced by all possible parameters **x**, and
190 ensures that the left-hand side of Eq. (2) integrates to 1. $P(\mathbf{x}|\mathbf{y})$ is termed the Bayesian *posterior*,
191 and describes the probability that a set of input parameters **x** produced a given precipitation
192 distribution **y**.

193 As mentioned earlier, a brute force calculation of the above probabilities for all
194 combinations of the six input parameters **x** is computationally intractable. The MCMC algorithm
195 reduces the computational burden by constructing a *guided random walk* that samples the
196 posterior probability distribution $P(\mathbf{x}|\mathbf{y})$. The random walk, a Markov process, consists of
197 randomly generated (Monte Carlo) test values of **x**, represented in the vector $\hat{\mathbf{x}}$. The walk is
198 guided by knowledge of the desired precipitation distribution **y**, with uncertainty determined by
199 $P(\mathbf{y}|\mathbf{x})$. Each test value of $\hat{\mathbf{x}}$, accompanied by a CM1 simulation, is referred to as an *iteration*;
200 multiple iterations make up a Markov chain. In each MCMC iteration, the following steps are
201 taken (flowchart shown in Fig. 4).

202 1. Candidate values for all parameters in $\hat{\mathbf{x}}$ are randomly drawn from a *proposal*
203 *distribution* $q(\hat{\mathbf{x}}, \mathbf{x}_i)$ centered on the current set of parameters $\mathbf{x}_i$. The proposal
204 distribution in this case is defined to be uncorrelated Gaussian, and the proposal variance
205 determines the size of perturbations to $\mathbf{x}_i$ in the Markov chain. The variance of the
206 proposal distribution is an adjustable parameter in the MCMC algorithm, and is tuned
207 during an adaptive *burn-in* period at the beginning of the chain to strike a balance
208 between efficient (large moves) and thorough (small moves) sampling of the control

variables. Parameter sets generated during the burn-in phase are not included in the posterior distribution.

2. CM1 simulates a precipitation distribution $\hat{\mathbf{y}} = f(\hat{\mathbf{x}})$ using the new $\hat{\mathbf{x}}$ values, and the simulated precipitation distribution is compared with the desired distribution using the likelihood $P(\mathbf{y}|\mathbf{x})$. For a Gaussian likelihood,

$$P(\mathbf{y} \mid \hat{\mathbf{x}}) \propto \exp\left[-\frac{1}{2}(\mathbf{y}-\hat{\mathbf{y}})^T \Sigma_y^{-1}(\mathbf{y}-\hat{\mathbf{y}})\right] \quad (3)$$

where Σ_y is the precipitation error covariance matrix. In our case, we assume precipitation uncertainty is uncorrelated between regions, and as such Σ_y is a diagonal matrix of precipitation error variances.

3. The *acceptance ratio* (Tamminen and Kyrölä, 2001; Delle Monache et al. 2008; Posselt, 2013) determines whether the candidate $\hat{\mathbf{x}}$ will be accepted as a sample of the posterior probability distribution $P(\mathbf{x}|\mathbf{y})$. The acceptance ratio is defined as:

$$\rho(\mathbf{x}_i, \hat{\mathbf{x}}) = \frac{P(\hat{\mathbf{y}} \mid \hat{\mathbf{x}})P(\hat{\mathbf{x}})q(\hat{\mathbf{x}}, \mathbf{x}_i)}{P(\mathbf{y}_i \mid \mathbf{x}_i)P(\mathbf{x}_i)q(\mathbf{x}_i, \hat{\mathbf{x}})} \quad (4)$$

This is the ratio between the probabilities on the right hand side of Bayes' relationship for the candidate $\hat{\mathbf{x}}$ (numerator in (4)) and the current $\mathbf{x}_i$ (denominator in (4)). Since our proposal distribution is symmetric, $q(\mathbf{x}_i, \hat{\mathbf{x}}) = q(\hat{\mathbf{x}}, \mathbf{x}_i)$ and equation (4) reduces to the ratio of prior and likelihood distributions. In addition, since the prior is identical everywhere within the acceptable parameter ranges, equation (4) depends only on the ratio of likelihoods.

4. If the candidate $\hat{\mathbf{x}}$ produces a better fit to the desired precipitation distribution than $\mathbf{x}_i$ ($\rho > 1$), $\hat{\mathbf{x}}$ is *accepted*, or saved, as a sample in the Markov chain ($\mathbf{x}_{i+1} = \hat{\mathbf{x}}$). If the

candidate $\hat{\mathbf{x}}$ does not produce an improved fit ($\rho < 1$), a test value is drawn from a Uniform (0,1) distribution. If this test value is less than the acceptance ratio, the candidate $\hat{\mathbf{x}}$ is saved as a sample in the Markov chain (this is termed *probabilistic acceptance*); if not, it is *rejected*, $\mathbf{x}_i$ is stored as another sample, and new candidate $\hat{\mathbf{x}}$ values are drawn using the proposal distributions described in step 1.

The coin-flip style comparison between the acceptance ratio and a Uniform random variable used in the probabilistic acceptance procedure allows the algorithm to preferentially sample high-probability regions of posterior parameter space, avoid very low probability regions, and appropriately sample the parameter space in between. Altogether, the MCMC-generated sample of the posterior probability completely characterizes the solution to Eq. (2). Sequential iterations of the MCMC process constitute a *Markov chain*, and the MCMC algorithm may be constructed to use multiple chains to explore the parameter space. This study employed 15 chains, and the MCMC algorithm is similar to those described in Delle Monache et al. (2008), Posselt and Vukicevic (2010), Posselt and Bishop (2012), and Posselt et al. (2014).

The parameters **x** that define the control case in this study are associated with the thermodynamic profile given in Fig. 2, and produce a moderate amount of orographic precipitation concentrated on the windward slope (Fig. 4a). Precipitation reaches an approximately steady state a few hours into the simulation (Fig. 4b). Parameter ranges were chosen to encompass a variety of thermodynamic and wind profiles and mountain geometries. The orographic Froude numbers (defined as $Fr = \frac{\overline{u}}{N_m H_{mtn}}$, Baines (1995), sec. 1.4) associated with each sample in the Markov chains range from positive values near zero, some of which are associated with blocked flow in the model, to values on the order of 50, associated with cases of small amplitude, standing mountain waves.

3. Results

3.1 One- and Two-Parameter Perturbation Experiments

Our ultimate goal is to determine which combinations of parameter values yield similar precipitation distributions as the control case, as well as to identify sensitivity and rapid transitions in the system. As mentioned above, this requires simultaneous perturbation of all six input parameters using the MCMC algorithm. Prior to performing such a study, it is useful to conduct a simplified analysis without using the MCMC algorithm, in which only one or two parameters are varied at a time and the rest held constant. This one- or two-at-a-time sensitivity analysis provides an initial estimate of the sensitivity of precipitation rate to changes in the control variables. As our focus is on upslope precipitation, we examine how precipitation rate in regions 2 and 3 (upwind slope; Fig. 1) changes with variation in each of the six parameters.

The slope of the precipitation rate *response function* (Fig. 5) indicates the degree of sensitivity to parameter changes: a steeper slope for a given change in a parameter reflects larger sensitivity to changes in that parameter. In addition to the response function slope, monotonicity and smoothness are important indicators of the parameter-precipitation rate relationship. A *non-monotonic* response, in which precipitation rate first increases with increasing parameter value, then decreases (or vice versa) at larger parameter values, means that scenarios exist in which two different parameter values will produce the same precipitation rate. A non-monotonic response also indicates a *non-unique* relationship between parameter and model output. A *non-smooth* response function, in which the model response changes suddenly around a particular parameter value, indicates the system experiences a rapid transition to a new state as the parameter increases beyond this value.

Examination of the response functions depicted in Fig. 5 reveals a range of behaviors in the model, from smooth, monotonic behavior to non-monotonic, non-smooth behavior. Precipitation rate increases monotonically with mountain height (Fig. 5a) in regions 2 and 3 until about 2.6 km, after which the rate stabilizes in region 2 and decreases in region 3. The non-monotonic change in precipitation rate with increasing mountain width (Fig. 5b) is due to the change in slope. As mountain width increases from 0 m, forced ascent occurs over a larger spatial region, leading to greater precipitation rate. However, as the width continues to increase with a fixed height, the slope decreases, resulting in smaller upward vertical motion and smaller precipitation rates. At large widths, precipitation rates are small and rain falls primarily upstream of the peak.

In general, the rain rate changes in a predictable and monotonic fashion with changes to the relative humidity (Fig. 5c): greater water vapor content leads to greater precipitation rate. Precipitation rates in region 3 exhibit a slight decrease at RH values greater than 95%, perhaps due to the fact that cloud and rain form farther upstream in an atmosphere with larger water vapor content, and precipitation rate increases in region 2 at the expense of region 3. Surface potential temperature (Fig. 5d) increases result in an approximately monotonic increase in precipitation rate in both upwind slope regions. If relative humidity is held constant as temperature increases, the atmospheric water vapor content will increase. As such, the precipitation response to warming of the profile is similar to the response to increases in RH. Precipitation rate response to moist stability (Fig. 5e) is non-monotonic; as moist stability increases past 4×10^{-5} s^{-2}, the increased resistance to vertical motion suppresses precipitation. Above a moist stability value of approximately 1.05×10^{-4} s^{-2}, precipitation does not occur. Examination of CM1 output indicates that, at these values, stagnation occurs at the upwind slope

298 and a back-propagating gravity wave suppresses cloud formation (as in MR05; Muraki and
299 Rotunno 2013).

300 Increases in wind speed (Fig. 5f) from 1 to ~15 m s^{-1} result in increases in precipitation
301 rate on the upwind slope (region 2) and mountain top (region 3). However, as wind speed
302 increases beyond 15 m s^{-1}, precipitation rate concentrates increasingly at the mountain top with
303 less on the upwind slope. This is consistent with advection of condensate farther downstream: for
304 a given environment and mountain geometry, larger wind advects precipitation farther
305 downstream, producing greater rainfall in region 3 at the expense of region 2. Interestingly,
306 precipitation rate in both regions 2 and 3 plummets at wind speeds of 23 and 24 m s^{-1},
307 respectively, before rapidly increasing again. This behavior is closely related to the properties of
308 mountain wave breaking, and will be discussed in more detail later.

309 In addition to one-at-a-time analyses, we can examine the joint response of two variables
310 at a time by holding four of the six parameters constant at their control values, while varying the
311 other two parameters incrementally across their defined ranges. In these experiments, the CM1
312 model was run for every combination of the two variable parameters, and the probability that
313 CM1 output was equal to the control precipitation in all six precipitation regions was then
314 calculated for each parameter combination. As mentioned above, we assume the prior probability
315 $P(\mathbf{x})$ is Uniform over the range of parameter values, and the precipitation rate likelihood $P(\mathbf{y}|\mathbf{x})$ is
316 Gaussian with 2 mm hr^{-1} standard deviation. Direct computation of the PDFs that result from
317 multiplying the prior and likelihood leads to a non-normalized solution to Bayes' Eq. (2).
318 Probabilities may be displayed as two-dimensional *joint parameter probability density functions*
319 *(PDFs)* that graphically display the conditional probability $P(\mathbf{x}|\mathbf{y})$. It is worth noting here that the
320 two-parameter experiments already present a more comprehensive view of the orographic

precipitation system and its sensitivity than previous modeling experiments. MR10 used CM1 to conduct 79 experiments, the highest number found in our search of the literature; here a single two-parameter PDF computation experiment includes 400 individual CM1 experiments (20 bins for each parameter).

Shown in Fig. 6 are three two-dimensional parameter PDFs from a set of three two-parameter experiments. In Fig. 6a, mean wind speed and moist stability (N_m^2) were varied while surface potential temperature, relative humidity, and mountain height and half-width were held constant at their control values. The control value for each varied parameter is indicated on the plots with a red line. The other plots follow a similar convention; Fig. 6b shows variations in potential temperature and RH, while Fig. 6c shows variations in mountain height and half-width. Brightest colors indicate the highest probability that the combination of parameters at that point produced a precipitation rate and distribution similar to the control distribution.

A first look shows a well-defined high-probability mode in wind speed and stability (Fig. 6a), centered about the control values; CM1 precipitation rate output is highly sensitive to changes in these parameters. In addition to a narrowly defined high probability region near the control values of N_m^2 and $\bar{u}$, a tail of high probability extends to high wind speeds at low stability values. The probability map indicates a positive correlation between wind speed and stability: increases in wind speed lead to increases in precipitation rate that may be compensated for by increasing the resistance to vertical motion (via an increase in stability). The model response to changes in relative humidity and surface potential temperature (Fig. 6b) has a large probability spread and diffuse gradients. At temperatures of 285-295 K, a decrease in RH, or available moisture, can compensate for increases in θ_{sfc} that may lead to larger precipitation rates. Above 295 K, however, the model instead develops a greater sensitivity to changes in RH and a reduced

sensitivity to changes in θ_{sfc}. Mountain height and half-width (Fig. 6c) display a well-defined high-probability mode, an indication that only parameter values similar to control values produce precipitation rates similar to control precipitation.

3.2 MCMC-Based Orographic Precipitation Analysis

While one- and two-parameter experiments yield information about the system and its complex relationships, a complete analysis of the combinations of parameters that produce a given rainfall distribution requires simultaneous perturbation of all six parameters. As mentioned above, such an exercise is intractable for more than a few parameters if it is done by brute force. The question of which parameter values produce a given distribution of precipitation in all six precipitation regions, and the associated sensitivities, can be addressed using Bayesian analysis via application of an MCMC algorithm. Early analysis of output from the MCMC algorithm indicated that approximately 100,000 simulations were sufficient to capture the salient properties of the parameter probability distribution. Although Haario et al. (1999) suggested only 20,000 samples were required to sample a multivariate 8-dimensional Gaussian distribution, we ran the MCMC experiment until it had produced more than one million runs of the CM1 model. The results comprise a thorough statistical sample that spans the complicated posterior distribution shown by univariate and bivariate sensitivity experiments, as well as a rich repository of CM1 output for further analysis. We computed the R-statistic ($\hat{R}$, Gelman et al. 2004), comparing within-chain variance to between-chain variance, to diagnose whether the 15 MCMC chains converged to sampling a stationary posterior distribution. A value of $\hat{R} < 1.1$ for each parameter generally indicates sufficient mixing and convergence. As shown in Fig. 7, all parameters exhibit $\hat{R} < 1.1$ after about 40,000 samples per chain, and $\hat{R} \leq 1.05$ by the time sampling ends.

MCMC produces a posterior probability distribution with variability in all 6 input parameters. Because it is challenging to visualize a 6-dimensional space, we present the PDF obtained from MCMC in the form of 2-dimensional marginal probability distributions for each pair of parameters (Fig. 8). Probabilities displayed in each 2-dimensional plot have been integrated over the other 4 dimensions, which may cause the highest probability regions to center on parameter combinations other than the control values. The probability maps displayed in Fig. 8 may be interpreted in the same way as the probability maps described in section 3.1 (Fig. 6).

Precipitation rates consistent with the control simulation occur with nearly equal probability for a large range of RH values. Conversely, the model expresses the greatest precipitation rate sensitivity to mean wind speed, static stability, and mountain geometry, as reflected in the well-defined probability modes and small dispersion. Taller orography and steeper slopes impede moist ascent, and as impediments become larger, moist stability and latent heating become increasingly important influences on the properties of the forced ascent. In addition, wind speed, moist stability, and the depth of air being lifted all affect hydrometeor growth, as well as location and amount of precipitation reaching the ground. Stagnation upwind of the mountain may result in convergence and precipitation upstream. However, if air parcels move too quickly, clouds may encounter leeward subsidence before precipitation has the chance to fall (Sawyer 1956; Smith 1979, 2006).

These plots also highlight parameter inter-relationships, most notable in the 2D covariance between mean wind speed and moist stability (Fig. 8a); wind speed and mountain height (Fig. 8g); wind speed and half-width (Fig. 8k); and height and half-width (Fig. 8o). An increase in mean wind speed is positively related to an increase in moist stability, and the same can be said for mean wind speed and width. Therefore, increasing the moist stability (making air

389 less susceptible to ascent) and increasing the mountain width (resulting in a shallower slope) can
390 compensate for increases in wind speed that cause higher precipitation rates. On the other hand,
391 increases in wind speed are negatively related to increases in mountain height. The same
392 relationship exists between mountain height and half-width. Decreasing mountain height and
393 reducing the amount of lift provided by terrain may compensate for larger precipitation rates
394 caused by increasing wind speed. Increasing precipitation rate by making a taller mountain can
395 be tempered by decreasing the half-width; the steeper slope may induce blocking or may favor
396 the advection of rainfall on the downslope and decrease the precipitation amount upstream.
397 An elongated high-probability region in the potential temperature and moist stability PDF
398 (Fig. 8c) implies that precipitation rate will remain constant for increasing temperature if moist
399 stability decreases simultaneously. However, upon close inspection the MCMC experiment also
400 reveals a secondary probability structure in a region of cool potential temperature and small
401 moist stability (283 K, 2×10^{-5} s^{-2}), indicating that multiple discrete combinations of surface
402 potential temperature and moist stability may produce similar precipitation rates. The complex
403 sensitivity of precipitation to surface potential temperature probably depends on the fact that the
404 latter controls both saturated and dry stability (Kirshbaum and Smith 2008). In fact, much of the
405 flow may desaturate over time (see e.g. Fig. 9), so dry stability (not fixed in this study) is
406 important as well as moist stability for wave dynamics (Jiang 2003, Cannon et al. 2012). Surface
407 potential temperature and moist stability are not the only parameters that exhibit multimodality;
408 prominent secondary probability modes can be seen in the marginal probability distributions of
409 surface potential temperature and moist stability (Fig. 8c), moist stability and RH (Fig. 8e), and
410 surface potential temperature and RH (Fig. 8f).
411 **4. Discussion**

From our one- and two-parameter sensitivity tests, as well as output from the MCMC experiment, we ascertain that precipitation rate has a complex dependence on changes in the control parameters: the overall response is rarely linear, and is at times non-smooth or non-monotonic. In the process of running the MCMC algorithm, output data from CM1 simulations corresponding to each MCMC iteration were stored. This database of simulated output can be used to examine the physics that give rise to the MCMC probability structures.

In our one-parameter sensitivity experiments, we noted that precipitation rate in regions 2 and 3 exhibited abrupt shifts when mean wind speed (Fig. 5f) was changed from 20-25 m/s with all other parameters held constant. Using the database of simulated output described above, we may compare CM1 output from our control case to output with the same input parameters, except for increased wind speed. Fig. 9 depicts CM1 output from the last hour of simulation for our control case (Figs. 9a,b), as well as for cases with the same input parameters but with higher wind speeds: 20 m/s (Figs. 9c,d), 21 m/s (Figs. 9e,f), 22 m/s (Figs. 9g,h), 23 m/s (Figs. 9i,j), 24 m/s (Figs. 9k,l), and 25 m/s (Figs. 9m,n). The left column depicts vertical cross sections of the flow and cloud distribution at the last hour of simulation (as in Fig. 4a), and the right column contains Hovmöller diagrams of rain rate for the entire simulation (as in Fig. 4b). For figures in the left column, recall that the thick black line outlines liquid precipitation, and the gray shading indicates the presence of cloud.

Recall from our analysis of Fig. 5f that the precipitation rate on the upwind slope (region 2) generally increases with increasing wind speed until about 20 m/s, decreases rapidly until 23 m/s, and increases dramatically again after. The upwind top of the mountain (region 3) exhibits a similar response; precipitation rate increases until 22 m/s, decreases rapidly, and starts increasing again at 25 m/s. The Hovmöller diagrams in Fig. 9 show ever-increasing precipitation rates on

435 the upwind slope of the mountain. A close examination of the vertical cross-sections, however,
436 shows that, for wind speeds of 20-23 m/s, increasing wind speeds result in more surface
437 precipitation near the mountain top, reducing the precipitation rate in region 2. A change occurs
438 when wind speeds reach 24 m/s; surface precipitation spreads out again along the upwind slope,
439 returning precipitation to region 2 at the expense of region 3. It is at this wind speed that the
440 precipitation distribution closely resembles that of the control case. As wind speeds continue to
441 increase to 25 m/s and beyond, precipitation rate increases as it did before.

442 It is notable that, while the precipitation distribution at $\bar{u}$ = 24 m/s was similar to that of
443 the control case (with $\bar{u}$ = 13 m/s), the flow and cloud distribution in the higher wind case were
444 entirely different, exhibiting a pronounced downstream breaking mountain wave. This reinforces
445 the possibility of two (or more) distinct sets of solutions that produce similar precipitation in
446 very different atmospheres, which we noted in the MCMC results (notably in Fig. 8c). The most
447 prominent high-probability mode (elongated probability region, Fig. 8c) corresponds to our
448 control case, defined by the parameter values listed in Table 1. Fig. 10a displays a vertical cross
449 section at the last hour of the control simulation, as in Fig. 4a. Wind speed increases as air flows
450 down the lee slope of the mountain, and a small amplitude mountain wave is evident above the
451 mountain peak. The second high-probability mode corresponds to the secondary high-probability
452 region of Fig. 8c, and has the following combination of parameter values: mean wind speed is 17
453 m s^{-1}, N_m^2 is $2x10^{-5}$ s^{-2}, surface potential temperature is 283 K, relative humidity is 95%,
454 mountain height is 2.75 km, and mountain half-width is 20 km. A vertical cross-section at the
455 last hour of the secondary high-probability mode simulation is presented in Fig. 10b. While
456 liquid precipitation reaches the surface in approximately the same location as in the control case,
457 similarities to the control case end there. The secondary high-probability mode exhibits a large

upstream cloud shield and an intense downslope wind storm. A breaking mountain wave propagates vertically downstream of the mountain top, and another tongue of precipitation reaches nearly to the ground far downstream. While leeside effects of this magnitude are uncommon, and likely exaggerated due to necessary model simplifications, they are meteorologically relevant (Seibert 1990, Zängl and Hornsteiner 2007).

In addition to examining the differences in atmospheric flow, cloud, and precipitation between the control case and a secondary high probability mode, it is useful to explore whether the atmosphere associated with the secondary high-probability mode exhibits similar sensitivity to changes in profile and mountain shape. To do this, we conduct two-parameter perturbation experiments identical to those described in section 3.1, but with the modal parameter values described in the previous paragraph used as the baseline instead of our control case parameters. Figs. 11a-c (top row) recall the 2D PDFs from the control case, whereas Figs. 11d-f show the 2D PDFs from the secondary high-probability mode.

The secondary high-probability mode PDFs take on a different probability structure than the PDFs from the control case. Multiple probability structures in wind speed and moist stability (Fig. 11d) are more defined and separated; on the other hand, the well-defined probability region in mountain height and half-width (Fig. 11f) has shrunk, implying an even greater sensitivity to those parameters. While the PDFs express nearly no sensitivity to relative humidity (Fig. 11e), there is a pronounced difference in potential temperature compared to the control case: potential temperature exhibits a distinctly bivariate probability structure. The atmospheric and probabilistic diversity between the control case and the secondary high-probability MCMC mode capture the complexity of this system—two distinct atmospheric soundings and mountain geometries with very different sensitivity structure produce nearly the same precipitation rate.

Finally, in addition to examining the bulk sensitivity and probability structure associated with changes in one or two parameters at a time, the computations performed in this study may be used to produce a first assessment of the required degree of accuracy for precipitation measurements. In order to determine how accurate measurements must be to constrain the relationships between precipitation and input parameters, we examine the change in parameter PDFs with changes in observational error. The error used in this study is Gaussian with a 2 mm hr^{-1} standard deviation (Figs. 12d-f, as in Fig. 6). Reducing the standard deviation by a factor of 0.5 to 1 mm hr^{-1} (Fig. 12a-c) leads to a contraction in high probability regions. Any secondary high-probability modes are still present. However, algorithms that search for a unique probability mode would now, with increased observation accuracy, likely find the true solution. Inflating the error, for example to standard deviation of 5 mm hr^{-1} (Figs. 12g-i), greatly expands regions with already high probability, and allows more mass in lower-probability regions. The result is an increase in non-uniqueness, or distinct multiple modes with equivalent (near unity) probability. This in effect lessens the significance of primary probability modes and makes convergence difficult for algorithms that search for a unique solution. As noted in Posselt et al. (2008) and Posselt and Vukicevic (2010), adding information to observations by reducing the observation error does not change the functional response of model output to changes in the input: the probability structure is the same. However, our results indicate that increasing observation accuracy to 1 mm hr^{-1} would have, in this case, produced a clearly dominant solution.

5. Summary and Conclusions

Although the dynamics of orographic precipitation have been a focus of study for many years, recent terrain-induced flooding in highly populated areas highlight the necessity of advancement in scientific understanding of the orographic precipitation system. Orographic

504 precipitation occurs in many and varied flow regimes; our current study focuses on a moist stable
505 to moist neutral idealized scenario. The limitations associated with idealization are summarized
506 later in this section. In order to answer questions concerning the sensitivity of topographically
507 forced precipitation to environmental and mountain characteristics, we employed the CM1 cloud
508 system resolving model in conjunction with a Markov Chain Monte Carlo algorithm. MCMC
509 allows sampling of substantial parameter space in a robust and (relative to brute force sensitivity
510 analysis) computationally efficient manner, and the resulting joint parameter probability
511 distribution can be used to identify relationships between parameters and observations, sources
512 of model sensitivity, and the result of adjusting observation uncertainty. Our major conclusions
513 from this work are as follows.

514 1. The orographic precipitation system has a *non-unique solution*. The same surface
515 precipitation rate and distribution can be obtained with very different sounding, flow, and
516 terrain characteristics. These different mountain geometry and sounding characteristics
517 correspond to a secondary high-probability mode in the Bayesian posterior PDF, which has
518 an entirely different cloud shield, mountain wave, and downslope wind than the control case.
519 2. Sensitivity tests conducted using a secondary high-probability mode resulted in a *different*
520 *sensitivity profile* than the original control case. While all tests showed sensitivity to changes
521 in wind speed and moist Brunt-Väisälä frequency, CM1 sensitivity to changes in surface
522 potential temperature (and even relative humidity) depends on the specific sounding and
523 mountain geometry. Additionally, co-variability between wind speed and stability, as well as
524 mountain height and half-width, does not depend on the control variables. Co-variability or
525 relationship between temperature and relative humidity, however, is situation-dependent.

3. In certain flow regimes, CM1 displays *high sensitivity* to small changes in certain parameters, namely surface potential temperature and wind speed. A further examination of flow and thermodynamic structures in individual CM1 runs shows that these small parameter changes lead to large alterations in moist mountain wave structure and the associated surface precipitation rate.
4. Finally, *changes in observation uncertainty* affect the ability to obtain a unique flow configuration from a given precipitation rate and distribution. Improving precipitation constraint from 2 mm hr^{-1} to 1 mm hr^{-1} produced a dominant solution. Degrading the accuracy to 5 mm hr^{-1}, on the other hand, results in a loss of that unique solution.

While this research uses an MCMC algorithm to thoroughly explore the parameter space associated with idealized moist neutral orographic precipitation, we have not considered many of the key sources of variability that influence orographic precipitation. This simplification was intentional, as the goal of this research was to extend previous univariate sensitivity studies into the multivariate domain, and to demonstrate the utility of Bayesian MCMC methods for exploring relationships in a physical system. For simplicity, we have utilized the simplest cloud microphysical parameterization available in the CM1. The details of cloud particle interactions, and in particular ice and mixed phase processes, have a strong influence on the characteristics of orographic precipitation for both warm and cold-based clouds. Changes to the cloud particle size distributions and assumed ice particle shape influence settling velocities and particle population interactions, and as such have a significant effect on precipitation rate and distribution. Posselt and Vukicevic (2010) used the MCMC algorithm to explore cloud microphysical sensitivity in simulations of deep convection, and we plan to conduct similar experiments for orographic precipitation cases.

549 Our mountain geometry was highly idealized, utilizing an infinite ridge with no along-
550 ridge variability. In a stable flow regime, this configuration allows the use of quasi-2D
551 simulations, as the flow will not vary with location in a non-convective environment. However,
552 many studies of observed orographic rain and snowfall have shown that the presence of gaps in a
553 barrier lead to concentration of the flow (so-called *gap winds*) that exert an influence on both the
554 upwind and downwind precipitation via their influence on cross-mountain flow. We also
555 neglected the influence of wind shear, changes in land use, the associated differences in sensible
556 and latent heat flux, and surface friction, all of which may improve the physical realism of
557 simulations in future study. Additional experiments could be performed to examine the sets of
558 environmental and mountain geometry parameters consistent with precipitation rates
559 concentrated on the mountain top and downwind slope, along with their canonical flow
560 structures; we also plan to expand our study to include unstable and convective precipitation
561 cases, as in MR09, MR10, and Miglietta and Rotunno (2012, 2014), in addition to the moist
562 stable and neutral cases represented here. Consideration of convective environments will greatly
563 increase the complexity of our experiments, as previous research has clearly illustrated that
564 three-dimensional domains and high horizontal grid spacing are required to realistically represent
565 convective circulations.
566 *Acknowledgements:* The authors would like to acknowledge the National Center for Atmospheric
567 Research Graduate Visitor Program and the Warner Internship for Scientific Enrichment for their
568 generous support and guidance during the residence of Ms. Samantha Tushaus and Prof. Derek
569 Posselt. We also thank Dr. George Bryan for his assistance with CM1. The comments of three
570 reviewers served to greatly improve the presentation of our results. This work was supported by
571 National Science Foundation Physical and Dynamic Meteorology grant AGS 1005454.

572 **REFERENCES**

573 Baines, P.G., 1995: *Topographic Effects in Stratified Flows*. Cambridge University Press, 482
574 pp.

575 Barcilon, A., J.C. Jusem, and P.G. Drazin, 1979: On the two- dimensional hydrostatic flow of a
576 stream of moist air over a mountain ridge. *Geophys. Astrophys. Fluid Dyn*., **13**, 125– 140.

577 Bougeault, P., and Coauthors, 2001: The MAP Special Observing Period. *Bull. Amer. Meteor.*
578 *Soc.*, **82**, 433–462.

579 Bryan, G.H., and J.M. Fritsch, 2002: A benchmark simulation for moist nonhydrostatic
580 numerical models. *Mon. Wea. Rev.*, **130**, 2917-2928.

581 Bryan, G.H., J.C. Wynguard, and J.M. Fritsch, 2003: Resolution requirements for the simulation
582 of deep moist convection. *Mon. Wea. Rev.*, **131**, 2394-2416.

583 Buzzi, A., and L. Foschini, 2000: Mesoscale meteorological features associated with heavy
584 precipitation in the Southern Alpine Region. *Meteor. Atmos. Phys*., **72**, 131–146.

585 Cannon, D.J, D.J. Kirshbaum, and S.L Gray, 2012: Under what conditions does embedded
586 convection enhance orographic precipitation? *Q. J. R. Meteor. Soc.*, **138**: 391-406.

587 Colle, B.A., 2004: Sensitivity of orographic precipitation to changing ambient conditions and
588 terrain geometries: An idealized modeling perspective. *J. Atmos. Sci*., **61**, 588–606.

589 Deardorff, J.W., 1980: Stratocumulus-capped mixed layer derived from a three-dimensional
590 model. *Bound. Layer. Meteor.*, **18**, 495-527.

591 Delle Monache, L., and Co-authors, 2008: Bayesian inference and Markov Chain Monte Carlo to
592 reconstruct a contaminant source at continental scale. *J. Appl. Meteor. Climatol.*, **47**,
593 2600-2613.

594 Doswell, C.A., III, C. Ramis, R. Romero, and S. Alonso, 1998: A diagnostic study of three heavy
595 precipitation episodes in the western Mediterranean. *Wea. Forecasting*, **13**, 102–124.

596 Douglas, C.K.M., and J. Glasspoole, 1947: Meteorological conditions in orographic rainfall in
597 the British Isles. *Q.J.R. Meteor. Soc*., **73**, 11–38.

598 Durran, D. R., and J. B. Klemp, 1982: The effects of moisture on trapped lee waves. *J. Atmos.*
599 *Sci*., **39**, 2490–2506.

600 Durran, D. R., and J. B. Klemp, 1983: A compressible model for the simulation of moist
601 mountain waves. *Mon. Wea. Rev*., **111**, 2341–2361.

602 Gelman, A., J.B. Carlin, H.S. Stern, and D.B. Rubin, 2004: *Bayesian Data Analysis*, 2nd ed.
603 Chapman and Hall/CRC, 696 pp.

604 Haario, H., E. Saksman, and J. Tamminen, 1999: Adaptive proposal distribution for random walk
605 Metropolis algorithm. *Comp. Stat.*, **14**, 375-395.

606 Jiang, Q., 2003: Moist dynamics and orographic precipitation. *Tellus*, **55A**, 301-316.

607 Kessler, E., 1969: On the distribution and continuity of water substance in atmospheric
608 circulations. *Meteorol. Monogr.*, No. 32, Amer. Meteor. Soc., Boston, 84 pp.

609 Kingsmill, D., and co-authors, 2006: Overview of the Sierra Hydrometeorology Atmospheric
610 River Experiment (SHARE). *12th Conf. on Mountain Meteorology*, Santa Fe, NM, Amer.
611 Meteor. Soc., P1.1.

612 Kirshbaum, D.J., and R.B. Smith, 2008: Temperature and moist-stability effects on midlatitude
613 orographic precipitation. *Q. J. R. Meteor. Soc.*, **134**, 1183-1199.

614 Miglietta, M.M., and A. Buzzi, 2001: A numerical study of moist stratified flows over isolated
615 topography. *Tellus*, **53A**, 481– 499.

616 Miglietta, M.M., and R. Rotunno, 2005: Simulations of Moist Nearly Neutral Flow over a
617 Ridge. *J. Atmos. Sci.*, **62**, 1410–1427.

618 Miglietta, M.M., and R. Rotunno, 2006: Further Results on Moist Nearly Neutral Flow over a
619 Ridge. *J. Atmos. Sci.*, **63**, 2881–2897.

620 Miglietta, M.M., and R. Rotunno, 2009: Numerical Simulations of Conditionally Unstable Flows
621 over a Mountain Ridge. *J. Atmos. Sci.*, **66**, 1865–1885.

622 Miglietta, M.M., and R. Rotunno, 2010: Numerical Simulations of Low-CAPE Flows over a
623 Mountain Ridge. *J. Atmos. Sci.*, **67**, 2391–2401.

624 Miglietta, M. M., and R. Rotunno, 2012: Application of theory to observed cases of
625 orographically forced convective rainfall, *Mon. Wea. Rev.*, **140**, 3039-3053.

626 Miglietta, M. M., and R. Rotunno, 2014: Numerical simulations of sheared conditionally
627 unstable flows over a mountain ridge, *Mon. Wea. Rev.*, In Press.

628 Muraki, D.J., and R. Rotunno, 2013: Internal Gravity Waves in a Saturated Moist Neutral
629 Atmosphere. *J. Amost. Sci.*, **70**, 3693-3709.

630 Neiman, P.J., F.M. Ralph, A.B. White, D.E. Kingsmill, P.O.G. Persson, 2002: The Statistical
631 Relationship between Upslope Flow and Rainfall in California's Coastal Mountains:
632 Observations during CALJET. *Mon. Wea. Rev.*, **130**, 1468–1492.

633 Neiman P. J., L.J. Schick, F.M. Ralph, M. Hughes and G.A. Wick, 2011: Flooding in western
634 Washington: The connection to atmospheric rivers. *J. Hydrometeor.*, **12**, 1337-1358.

635 Posselt, D.J., T.S. L'Ecuyer, and G.L. Stephens, 2008: Exploring the Error Characteristics of
636 Thin Ice Cloud Property Retrievals Using a Markov Chain Monte Carlo Algorithm.
637 *Geophys. Res. Lett.*, **113**, D24206.

638 Posselt, D.J., and T. Vukicevic, 2010: Robust Characterization of Model Physics Uncertainty for
639 Simulations of Deep Moist Convection. *Mon. Wea. Rev.*, **138**, 1513-1535.

640 Posselt, D.J., and C.H. Bishop, 2012: Nonlinear parameter estimation: Comparison of an
641 Ensemble Kalman Smoother with a Markov Chain Monte Carlo algorithm. *Mon. Wea.*
642 *Rev.*, **140**, 1957-1974.

643 Posselt, D.J., 2013: Markov Chain Monte Carlo Methods. *Theory and Applications in Data*
644 *Assimilation for Atmospheric, Oceanic and Hydrologic Applications Vol. II*, S. K. Park
645 and L. Xu, Eds., Springer, 59-87.

646 Posselt, D.J.**,** D. Hodyss, and C.H. Bishop, 2014: Errors in Ensemble Kalman Smoother
647 Estimates of Cloud Microphysical Parameters. Mon. Wea. Rev., **142,** 1631-1654.

648 Ralph F. M., P.J. Neiman, and G.A. Wick. 2004. Satellite and CALJET aircraft observations of
649 atmospheric rivers over the eastern North Pacific ocean during the winter of 1997/98.
650 *Mon. Wea. Rev*., **132**, 1721 – 1745.

651 Ralph, F.M., P.J. Nieman, and R. Rotunno, 2005: Dropsonde observations in low-level jets over
652 the northeastern Pacific Ocean from CALJET-1998 and PACJET-2001: Mean vertical-
653 profile and atmospheric-river characteristics. *Mon. Wea. Rev*., **133**, 889–910.

654 Ralph, F.M., and M.D. Dettinger, 2011: Storms, Floods, and the Science of Atmospheric Rivers.
655 EOS, Transactions, *Amer. Geophys. Union*, **92**, 265-266.

656 Rotunno, R. and R. Ferretti, 2003: Orographic effects on rainfall in MAP cases IOP 2b and IOP
657 8. *Q.J.R. Meteor. Soc*., **129**, 373–390.

658 Rotunno, R. and R.A. Houze, 2007: Lessons on orographic precipitation from the Mesoscale
659 Alpine Programme. *Q.J.R. Meteor. Soc.*, **133**, 811–830.

660 Rutz, J.J., W.J. Steenburgh, and F.M. Ralph, 2014: Climatological Characteristics of
661 Atmospheric Rivers and Their Inland Penetration over the Western United States. *Mon.*
662 *Wea. Rev.*, **142**, 905-921.

663 Sarker, R.P., 1967: Some modifications in a dynamical model of orographic rainfall. *Mon. Wea.*
664 *Rev*., **95**, 673–684.

665 Sawyer, J.S., 1956: The physical and dynamical problems of orographic rain. *Wea.*, **11**, 375-381.

666 Schultz, D. M., and Co-authors, 2002: Understanding Utah Winter Storms: The Intermountain
667 Precipitation Experiment. *Bull. Amer. Meteor. Soc*., **83**, 189-210.

668 Seibert, P., 1990: South Foehn Studies Since the ALPEX Experiment. *Meteor. Atmos. Phys.*, **43**,
669 91-103.

670 Smith, R.B., 1979: The influence of mountains on the atmosphere. *Advances in Geophysics Vol.*
671 *21*, B. Saltzman, Ed., Academic Press, 87-230.

672 Smith, R.B., 2006: Progress on the theory of orographic precipitation. *GSA Spec. Pap.*, **398**, 1-
673 16.

674 Stoelinga, M.T., and co-authors, 2003: Improvement of Microphysical Parameterization Through
675 Observational Verification Experiment. *Bull. Am. Meteor. Soc.*, **84**, 1807-1826.

676 Tamminen, J., and E. Kyrölä, 2001: Bayesian solution for nonlinear and non-Gaussian inverse
677 problems by Markov Chain Monte Carlo method. *J. Geophys. Res.*, **106**, 14377-14390.

678 Vukicevic, T., and D. J. Posselt, 2008: Analysis of the Impact of Model Nonlinearities in Inverse
679 Problem Solving. *J. Atmos. Sci*., **65**, 2803-2823.

680 Zängl, G., and M. Hornsteiner, 2007: The exceptional Alpine south foehn event of 14-16
681 November 2002: a case study. *Meteor. Atmos. Phys.*, **98**, 217-238.
682

List of Tables

689

690 Table 1. Maximum and minimum values for all model input parameters, as well as value of each
691 parameter used in control case.

692

Parameter Description	Control	Min	Max	Symbol	Units
Mean wind speed	13	2	30	$\bar{u}$	$m\ s^{-1}$
Squared, Moist Brunt-Väisälä frequency	$4x10^{-5}$	$2.5x10^{-6}$	$2x10^{-4}$	N_m^2	s^{-2}
Surface potential temperature	292	280	300	θ_{sfc}	K
Relative humidity	0.95	0.8	1.0	RH	none
Mountain height	$2.35x10^3$	$3x10^2$	$3x10^3$	H_{mtn}	m
Mountain half-width	$3x10^4$	$5x10^3$	$1x10^5$	W_{mtn}	m

693
694

695

696 Table 2. Precipitation rate averaged over each precipitation region on the mountain during the
697 last hour of simulation in the control run.

698

	Region 1	**Region 2**	**Region 3**	**Region 4**	**Region 5**	**Region 6**
Averaged Precipitation Rate (mm hr^{-1})	2.70	5.49	7.74	1.87	$1.13x10^{-2}$	0.0

699

700
701

List of Figures

1. Visual depiction of the case study topography and the six precipitation bins.

2. Modeled skew-T diagram from CM1 depicting the atmosphere entering the westernmost (upwind) edge of the domain during the first hour in the control case. Wind speed is in units of m s^{-1}.

3. *(a)* X-Z cross-section of model domain during last hour of simulation. Cloud liquid water content shaded in gray: $0.01 < q_c < 0.1$ g kg^{-1} in light grey, $0.1 < q_c < 0.5$ g kg^{-1} in medium grey, and $q_c > 0.5$ g kg^{-1} in dark grey. Thick black contours outline regions of liquid precipitation greater than 0.2 g kg^{-1}. *U*- and *w*-direction streamlines are colored by *u*- wind component (m s^{-1}). *(b)* Hovmöller diagram of precipitation rate (mm hr^{-1}, shaded). Rain rate greater than 0.2 mm hr^{-1} contoured in black.

4. Flowchart illustrating the Markov chain Monte Carlo process.

5. Response of precipitation (mm hr^{-1}) to changes in each of the model input parameters. Red lines indicate the parameter value used in the control case. The solid line represents precipitation response in precipitation region 2 on the mountain, and the dashed line shows the response for precipitation region 3.

6. Two-dimensional joint PDFs of (*a*) wind speed and stability, (*b*) surface potential temperature and relative humidity, and (*c*) mountain height and half-width from a parameter perturbation experiment. Red lines indicate the parameter value used in the control case. Bright colors at any point imply a high probability that the parameter combination at that point produced precipitation output similar to the control output.

7. R-statistic ($\hat{R}$) values for each model input parameter, for successively greater numbers of samples.

8. Posterior two-dimensional marginal PDFs for all pairs of input parameters from the MCMC experiment. As in Fig. 5, red lines indicate the parameter value used in the control case. White solid and dashed lines contour the 68% and 95% probability mass, respectively. Bright colors at any point imply a high probability that the parameter combination at that point produced precipitation output similar to the control output.

9. Contours, shading, and colors as in Fig. 3. X-Z cross-sections of the model domain during last hour of simulation (*first column*). Hovmöller diagrams of precipitation rate (*second column*). Each row represents model output for varying wind speeds: 13 m s^{-1} (control case; *a*,*b*), 20 m s^{-1} (*c*,*d*), 21 m s^{-1} (*e*,*f*), 22 m s^{-1} (*g*,*h*), 23 m s^{-1} (*i*,*j*), 24 m s^{-1} (*k*,*l*), and 25 m s^{-1} (*m*,*n*).

10. Contours, shading, and colors as in Fig. 3a. *(a)* X-Z cross-section of control case. *(b)* X-Z cross-section of the second MCMC high-probability mode, as described in Section 4.

11. Contours, lines, and shading as in Fig. 5. The *first column* contains 2D joint PDFs of wind speed and stability; the *second column* contains 2D PDFs of surface potential

temperature and relative humidity; and the *third column* contains 2D PDFs of mountain height and half-width. The *first row* represents the control case; the *second row* represents the second MCMC high-probability mode.

12. Contours, lines, and shading as in Fig. 5. The *first column* contains 2D joint PDFs of wind speed and stability; the *second column* contains 2D PDFs of surface potential temperature and relative humidity; and the *third column* contains 2D PDFs of mountain height and half-width. The *first row* represents the control case with 1σ error; the *second row* represents the control case with 2σ error; and the *third row* represents the control case with 5σ error.

749

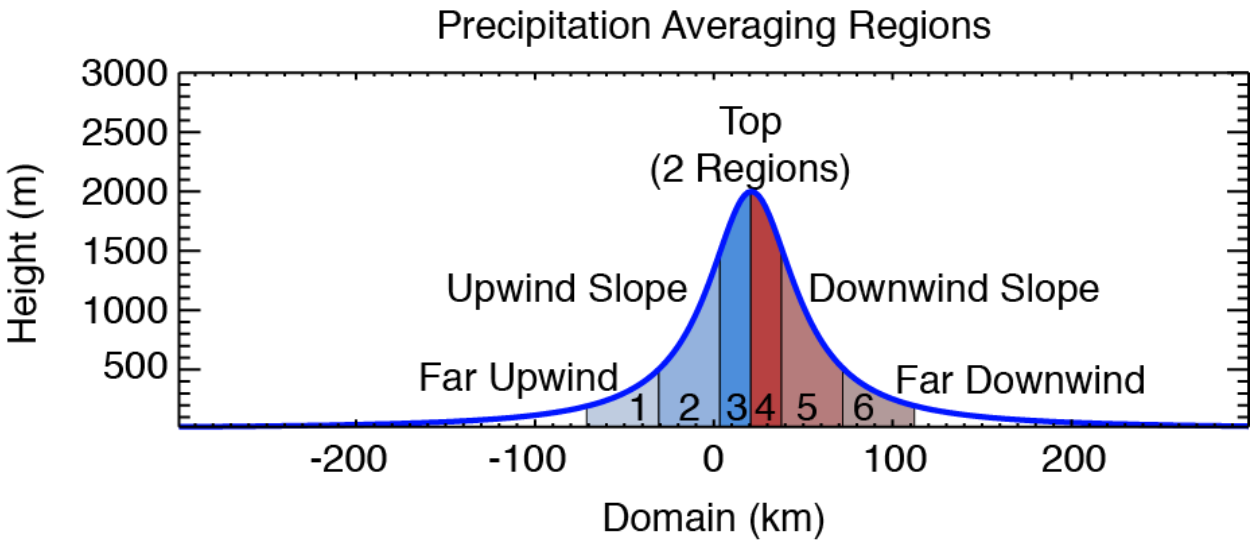

750

751 Figure 1. Visual depiction of the case study topography and the six precipitation bins.
752

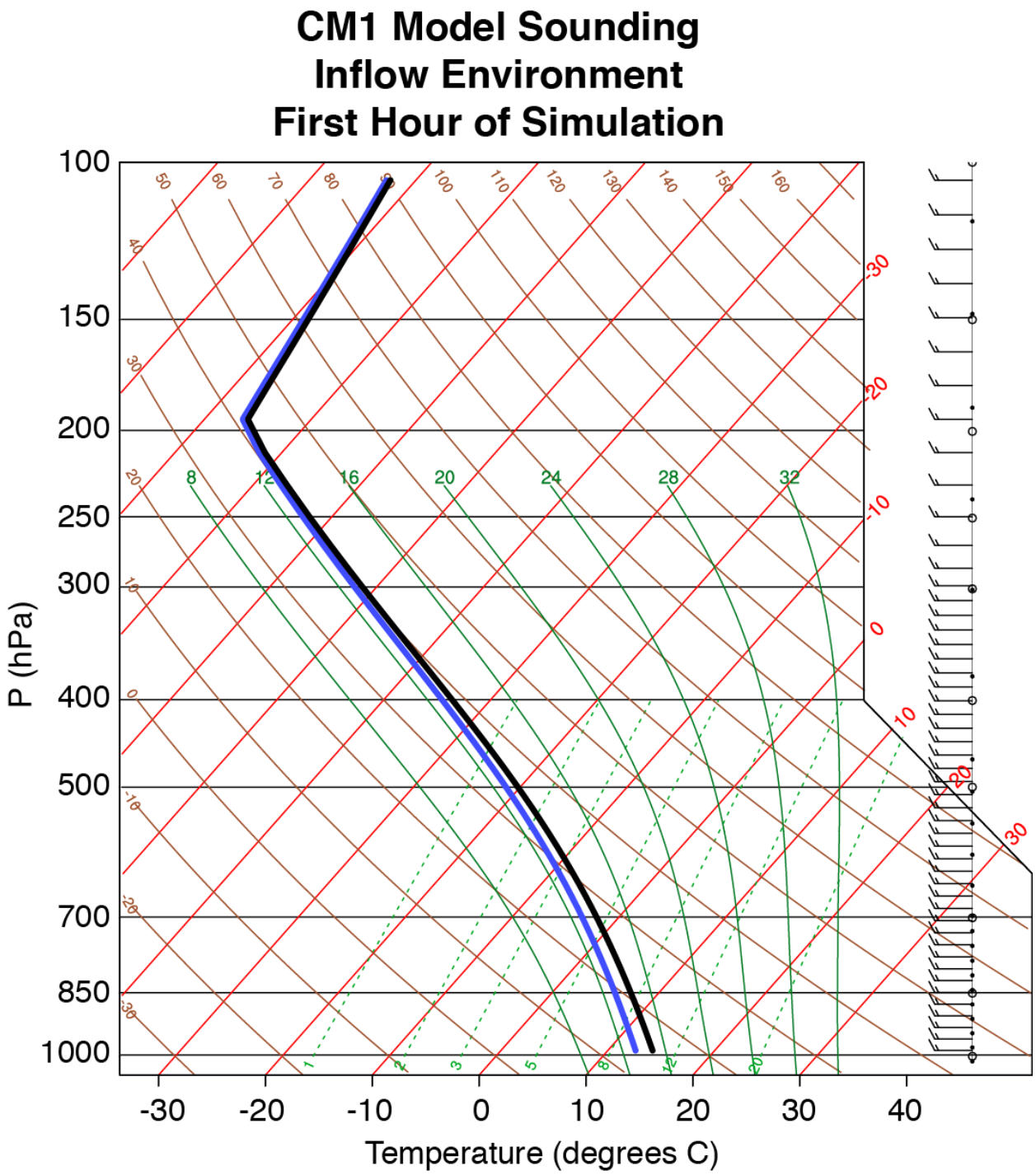

Figure 2. Modeled skew-T diagram from CM1 depicting the atmosphere entering the westernmost (upwind) edge of the domain during the first hour in the control case. Wind speed is in units of m s^{-1}.

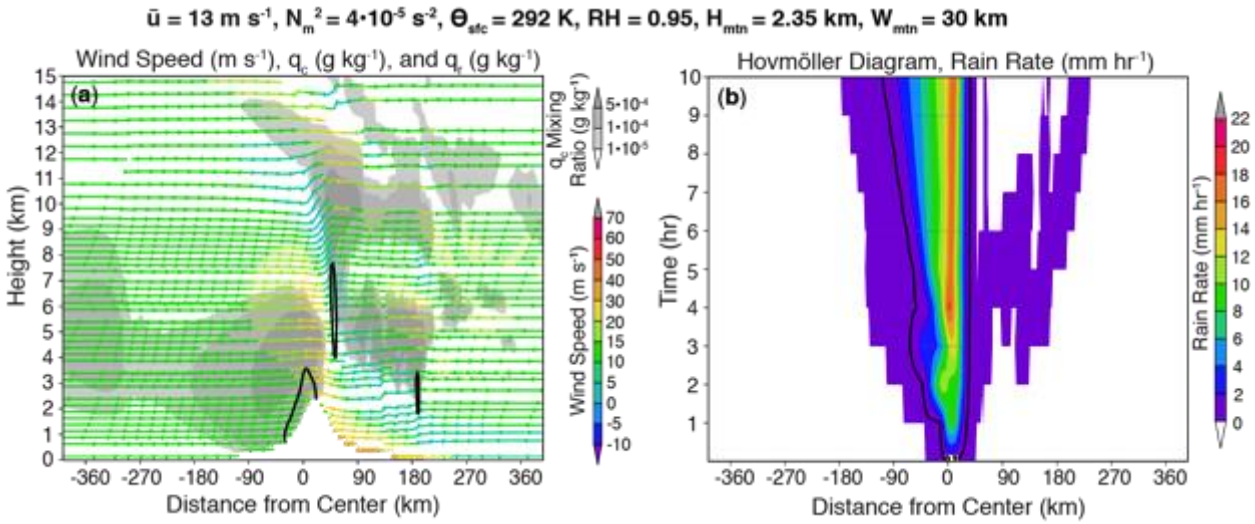

Figure 3. *(a)* X-Z cross-section of model domain during last hour of simulation. Cloud liquid water content shaded in gray: $0.01 < q_c < 0.1$ g kg^{-1} in light grey, $0.1 < q_c < 0.5$ g kg^{-1} in medium grey, and $q_c > 0.5$ g kg^{-1} in dark grey. Thick black contours outline regions of liquid precipitation greater than 0.2 g kg^{-1}. *U*- and *w*-direction streamlines are colored by *u*- wind component (m s^{-1}). *(b)* Hovmöller diagram of precipitation rate (mm hr^{-1}, shaded). Rain rate greater than 0.2 mm hr^{-1} contoured in black.

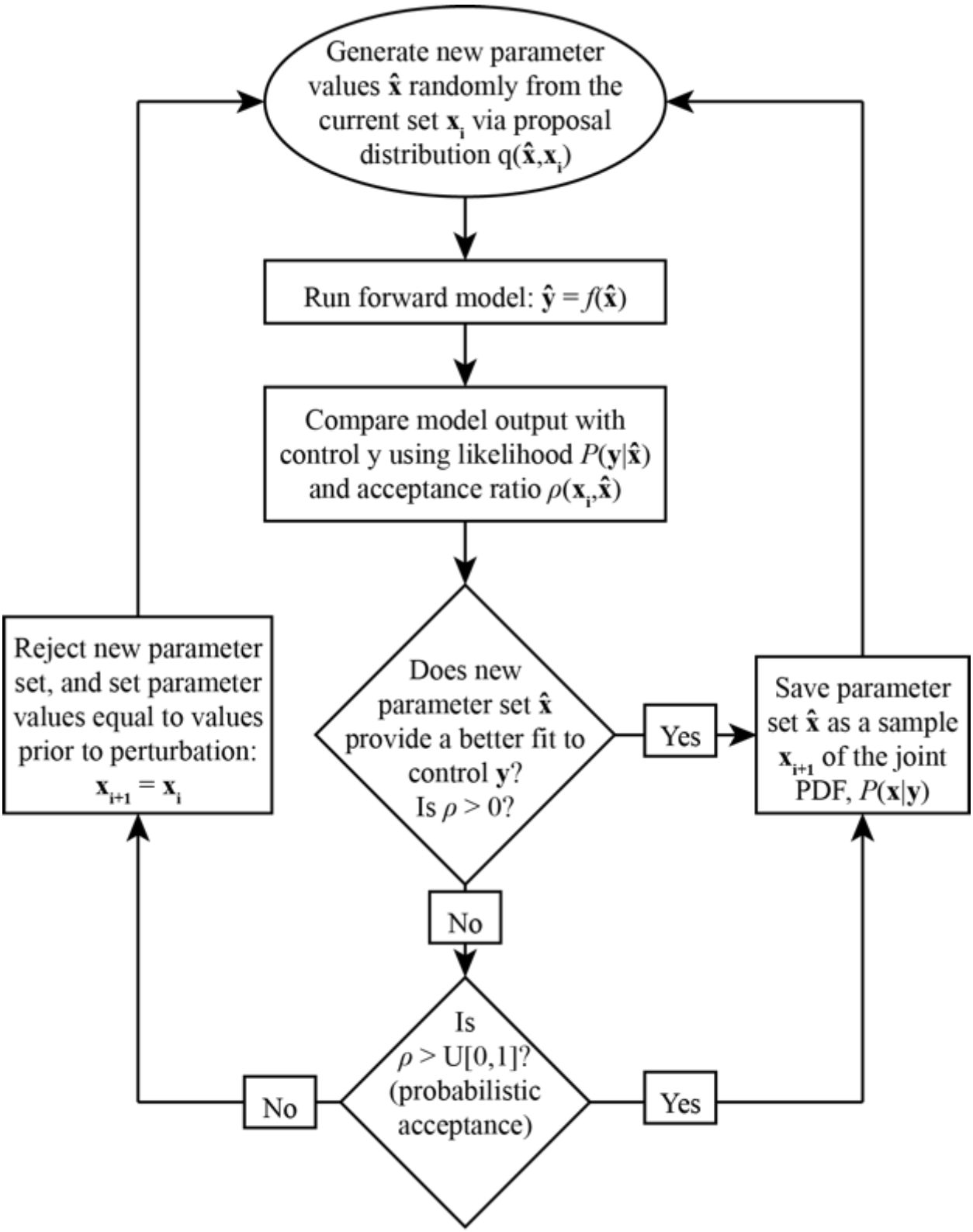

Figure 4. Flowchart illustrating the Markov chain Monte Carlo process.

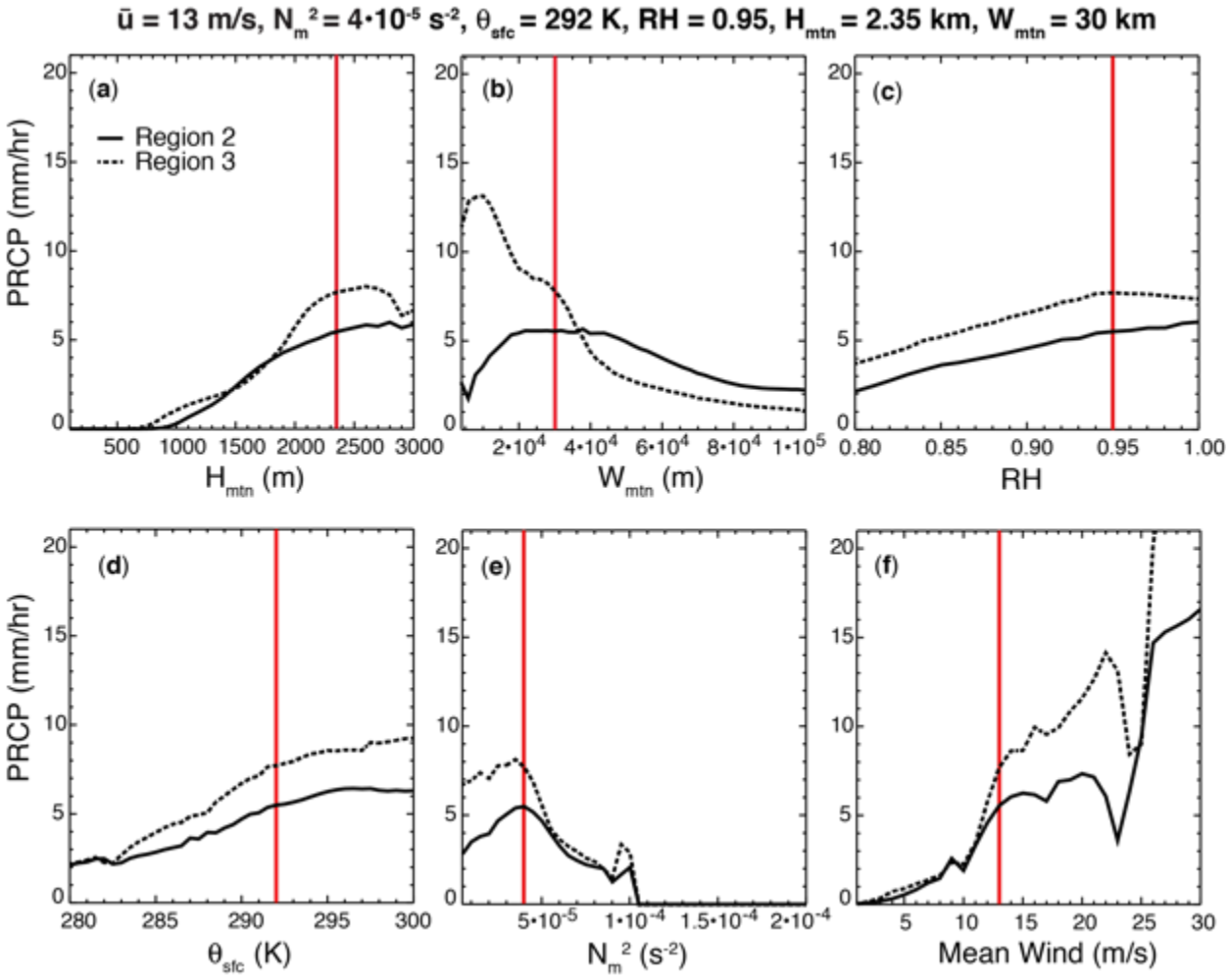

Figure 5. Response of precipitation (mm hr^{-1}) to changes in each of the model input parameters. Red lines indicate the parameter value used in the control case. The solid line represents precipitation response in precipitation region 2 on the mountain, and the dashed line shows the response for precipitation region 3.

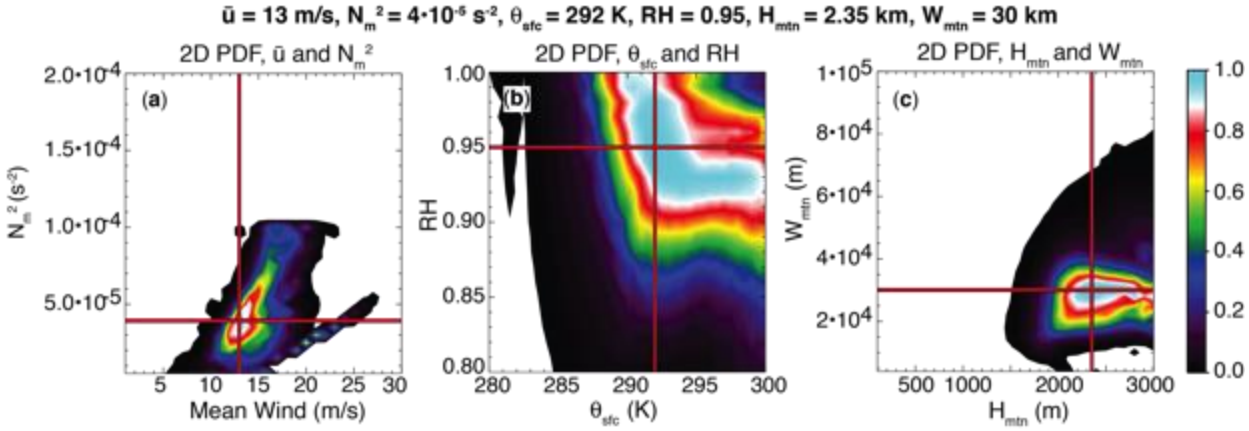

Figure 6. Two-dimensional joint PDFs of (*a*) wind speed and stability, (*b*) surface potential temperature and relative humidity, and (*c*) mountain height and half-width from a parameter perturbation experiment. Red lines indicate the parameter value used in the control case. Bright colors at any point imply a high probability that the parameter combination at that point produced precipitation output similar to the control output.

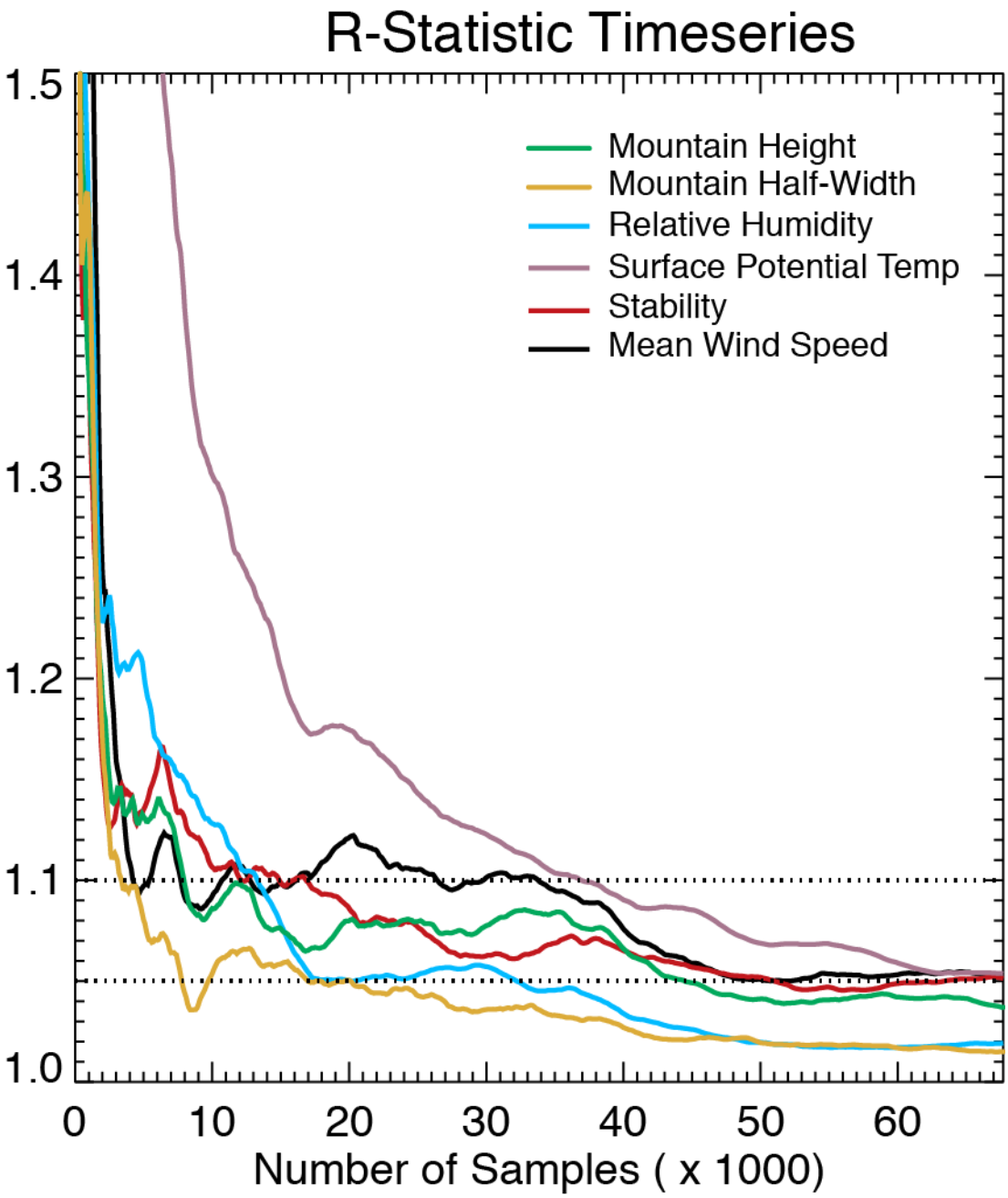

Figure 7. R-statistic ($\hat{R}$) values for each model input parameter, for successively greater numbers of samples.

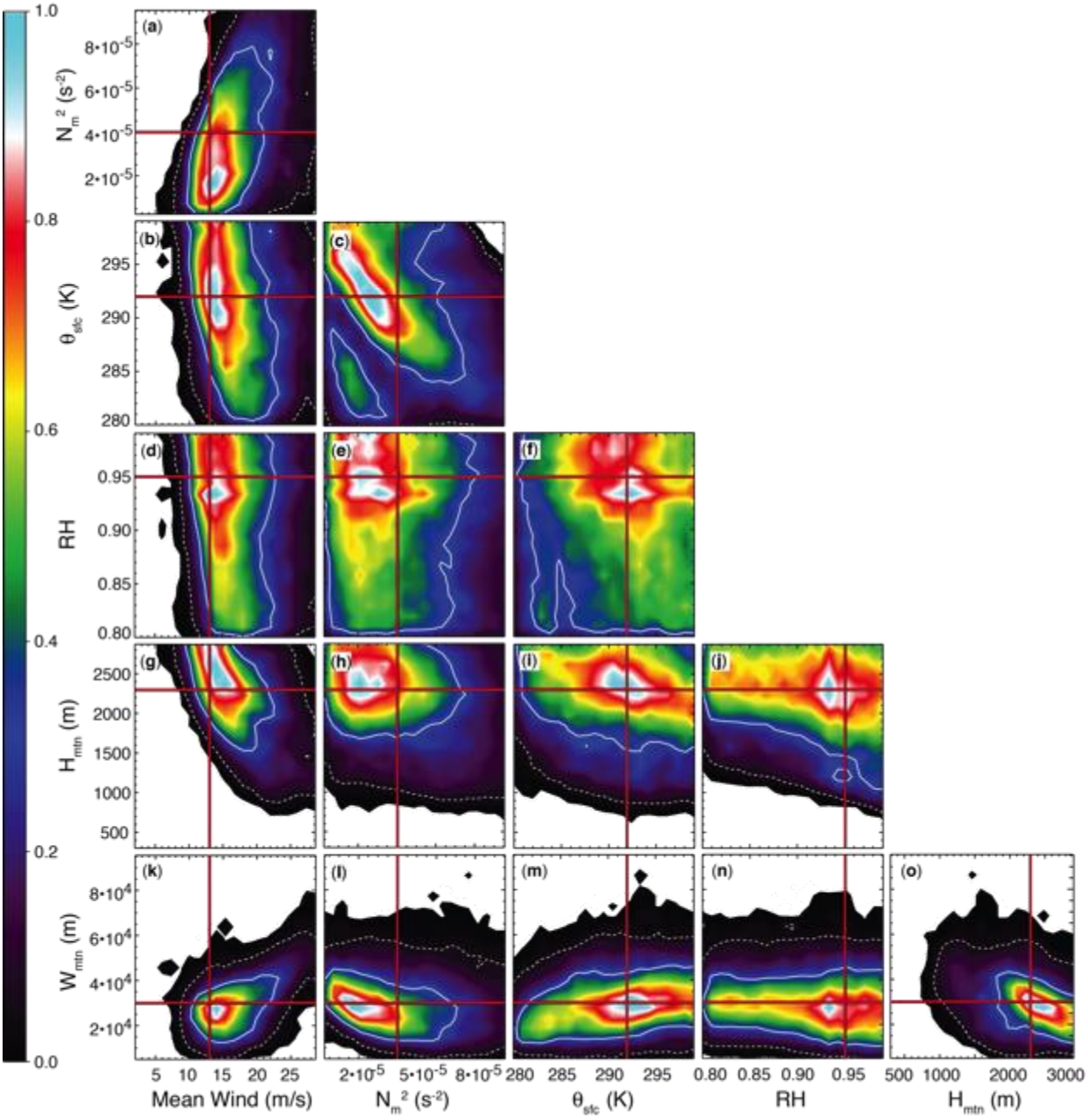

Figure 8. Posterior two-dimensional marginal PDFs for all pairs of input parameters from the MCMC experiment. As in Fig. 5, red lines indicate the parameter value used in the control case. White solid and dashed lines contour the 68% and 95% probability mass, respectively. Bright colors at any point imply a high probability that the parameter combination at that point produced precipitation output similar to the control output.

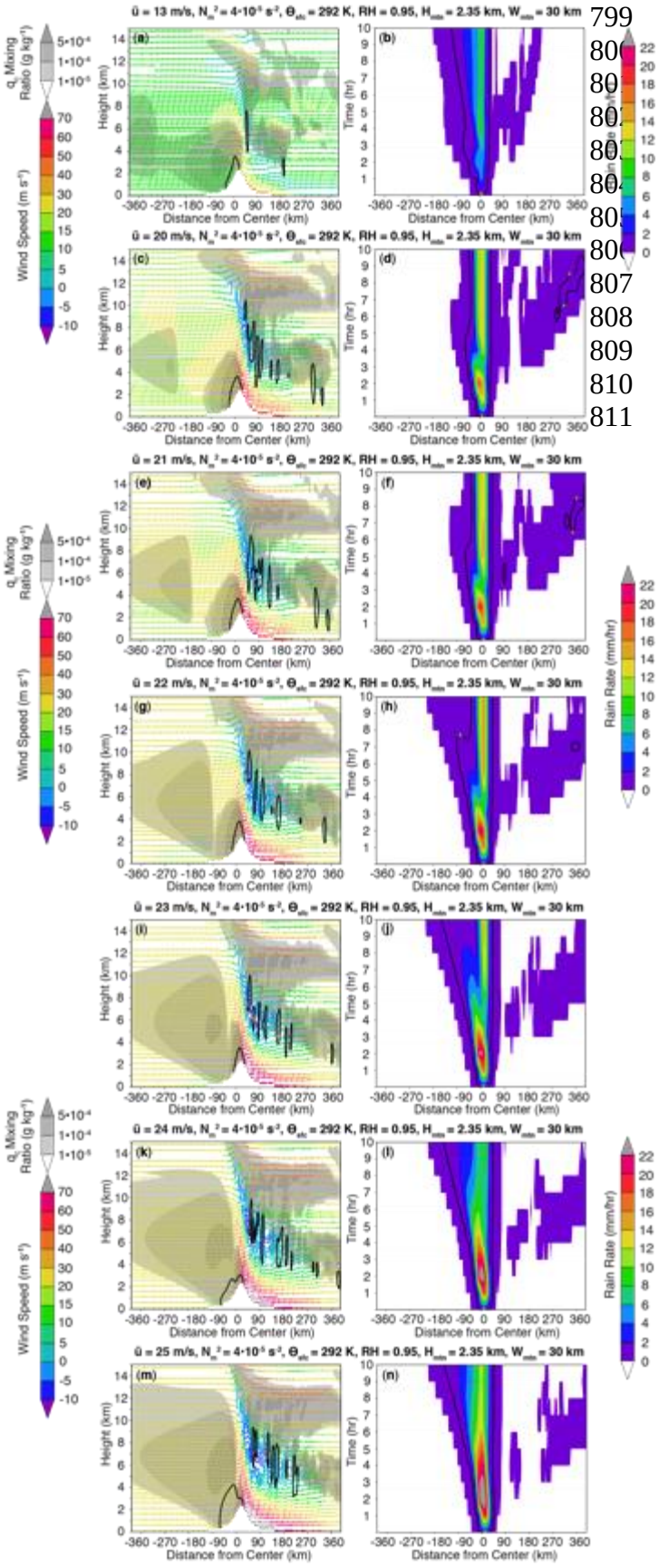

Figure 9. Contours, shading, and colors as in Fig. 3. X-Z cross-sections of the model domain during last hour of simulation (*first column*). Hovmöller diagrams of precipitation rate (*second column*). Each row represents model output for varying wind speeds: 13 m s^{-1} (control case; *a*,*b*), 20 m s^{-1} (*c*,*d*), 21 m s^{-1} (*e*,*f*), 22 m s^{-1} (*g*,*h*), 23 m s^{-1} (*i*,*j*), 24 m s^{-1} (*k*,*l*), and 25 m s^{-1} (*m*,*n*).

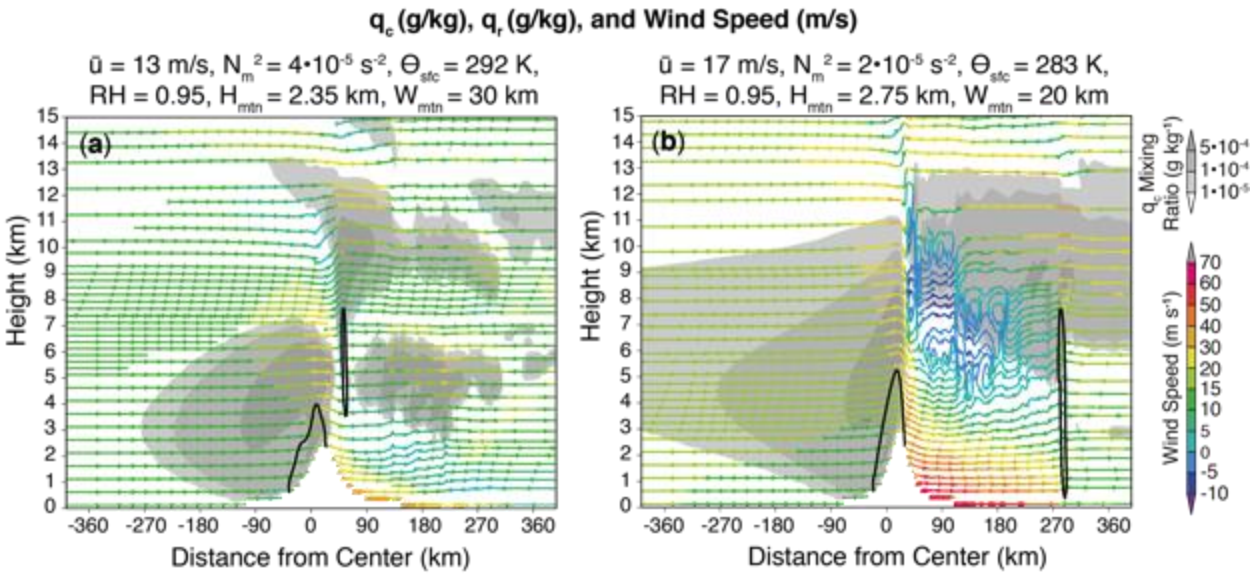

812

813 Figure 10. Contours, shading, and colors as in Fig. 3a. *(a)* X-Z cross-section of control case. *(b)*
814 X-Z cross-section of the second MCMC high-probability mode, as described in Section 4.

815
816

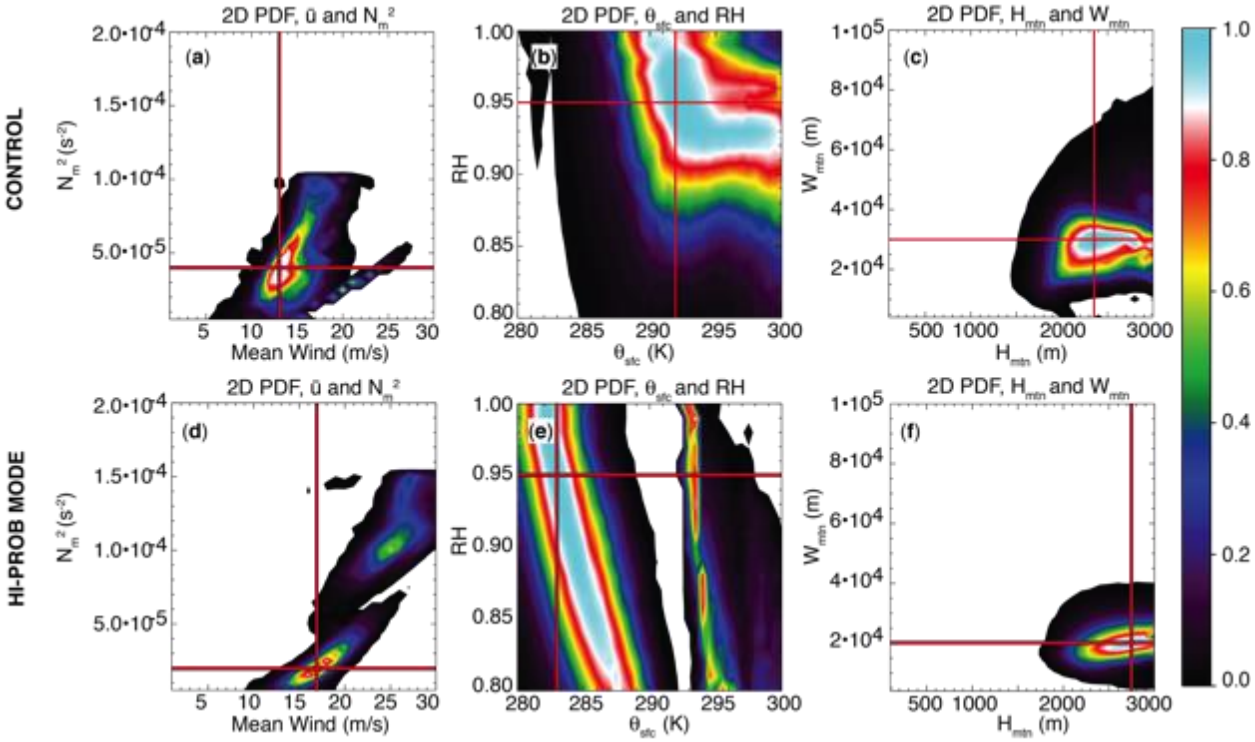

817

818 Figure 11. Contours, lines, and shading as in Fig. 5. The *first column* contains 2D joint PDFs of
819 wind speed and stability; the *second column* contains 2D PDFs of surface potential temperature
820 and relative humidity; and the *third column* contains 2D PDFs of mountain height and half-
821 width. The *first row* represents the control case; the *second row* represents the second MCMC
822 high-probability mode.
823

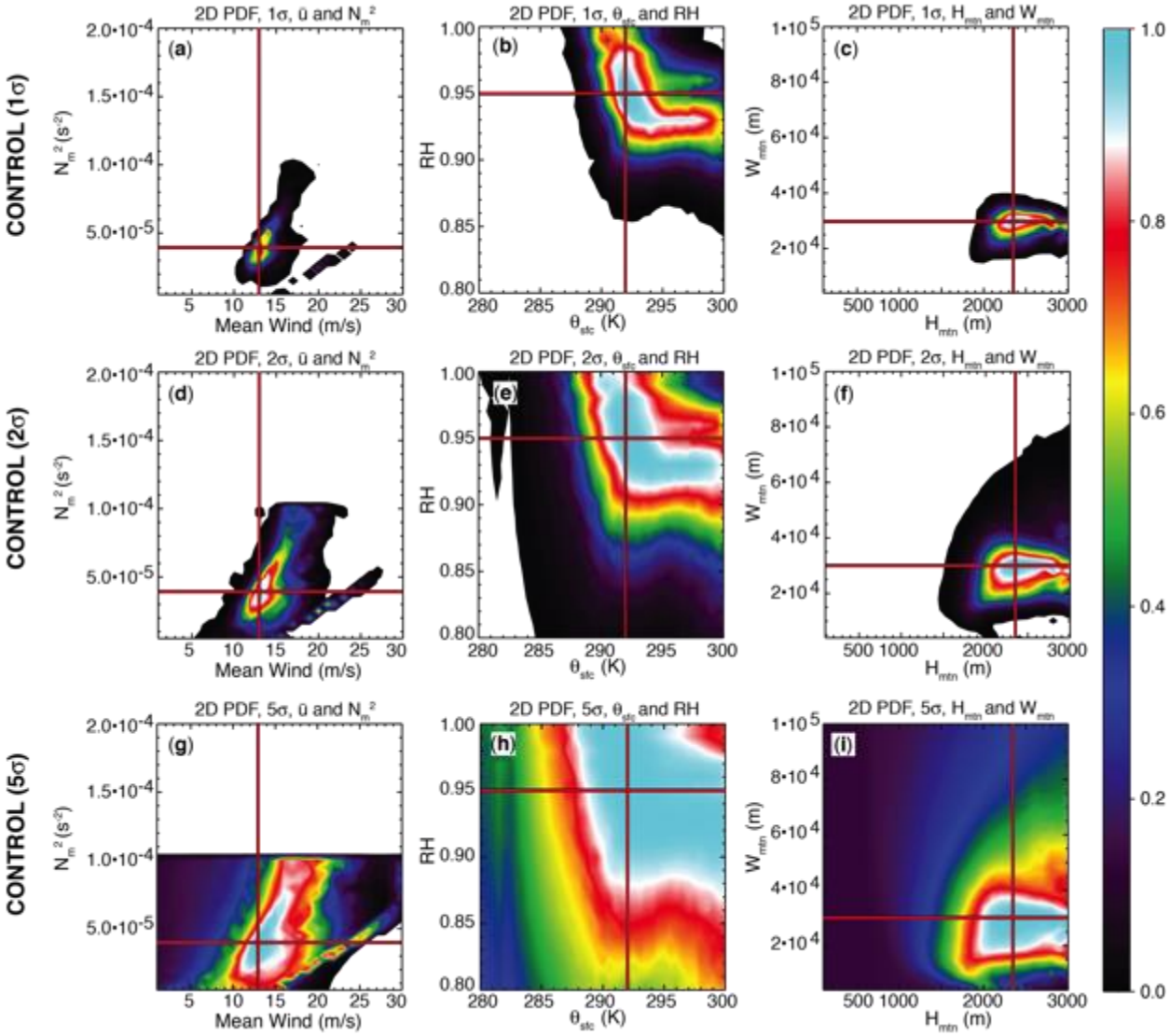

Figure 12. Contours, lines, and shading as in Fig. 5. The *first column* contains 2D joint PDFs of wind speed and stability; the *second column* contains 2D PDFs of surface potential temperature and relative humidity; and the *third column* contains 2D PDFs of mountain height and half-width. The *first row* represents the control case with 1σ error; the *second row* represents the control case with 2σ error; and the *third row* represents the control case with 5σ error.